Title
Cas1 and the Csy complex are opposing regulators of Cas2/3 nuclease activity

Journal
Proceedings of the National Academy of Sciences of the United States of America, 114(26)

ISSN
0027-8424

Authors
Rollins, MaryClare F
Chowdhury, Saikat
Carter, Joshua
et al.

Publication Date
2017-06-27

DOI
10.1073/pnas.1616395114

Peer reviewed

Cas1 and the Csy complex are opposing regulators of Cas2/3 nuclease activity

MaryClare F. Rollins[a], Saikat Chowdhury[b], Joshua Carter[a], Sarah M. Golden[a], Royce A. Wilkinson[a], Joseph Bondy-Denomy[c], Gabriel C. Lander[b], and Blake Wiedenheft[a,1]

[a]Department of Microbiology and Immunology, Montana State University, Bozeman, MT 59717; [b]Department of Integrative Structural and Computational Biology, The Scripps Research Institute, La Jolla, CA 92037; and [c]Department of Microbiology and Immunology, University of California, San Francisco, CA 94158

Edited by Jennifer A. Doudna, University of California, Berkeley, CA, and approved March 13, 2017 (received for review October 2, 2016)

The type I-F CRISPR adaptive immune system in *Pseudomonas aeruginosa* (PA14) consists of two CRISPR loci and six CRISPR-associated (*cas*) genes. Type I-F systems rely on a CRISPR RNA (crRNA)-guided surveillance complex (Csy complex) to bind foreign DNA and recruit a *trans*-acting nuclease (i.e., Cas2/3) for target degradation. In most type I systems, Cas2 and Cas3 are separate proteins involved in adaptation and interference, respectively. However, in I-F systems, these proteins are fused into a single polypeptide. Here we use biochemical and structural methods to show that two molecules of Cas2/3 assemble with four molecules of Cas1 ($Cas2/3_2$:$Cas1_4$) into a four-lobed propeller-shaped structure, where the two Cas2 domains form a central hub (twofold axis of symmetry) flanked by two Cas1 lobes and two Cas3 lobes. We show that the Cas1 subunits repress Cas2/3 nuclease activity and that foreign DNA recognition by the Csy complex activates Cas2/3, resulting in bidirectional degradation of DNA targets. Collectively, this work provides a structure of the Cas1–2/3 complex and explains how Cas1 and the target-bound Csy complex play opposing roles in the regulation of Cas2/3 nuclease activity.

CRISPR | Cas | Cas1 | Cas2/3 | type I-F

In response to viral infection, bacteria and archaea have evolved sophisticated adaptive immune systems that rely on CRISPR (clustered regularly interspaced short palindromic repeats) loci and a diverse set of CRISPR-associated (*cas*) genes (1–3). These immune systems operate in three stages: acquisition of foreign DNA, CRISPR RNA (crRNA) biogenesis, and target interference (4–6). During new sequence acquisition (stage 1), small pieces of foreign DNA (protospacers) are integrated into one end of the evolving CRISPR locus, resulting in a chronological molecular record of previously encountered foreign nucleic acids. This molecular record is transcribed, and the long pre-crRNA is processed into a library of mature crRNAs that assemble with Cas proteins into crRNA-guided surveillance complexes (stage 2) that detect and degrade invading DNA or RNA targets (stage 3).

Despite their common function in adaptive immunity, CRISPR-Cas systems are phylogenetically and functionally diverse. According to the most recent classification, CRISPR systems are divided into two classes, six types (types I–VI), and 19 subtypes (7, 8). Type I is the most common, consisting of seven subtypes (I-A to I-F, and I-U) that all rely on multisubunit crRNA-guided surveillance complexes for target detection, and a *trans*-acting effector protein called Cas3, which is required for target destruction (9–13). Cas3 proteins are typically composed of an amino-terminal histidine-aspartate (HD)-nuclease domain, fused to a carboxyl-terminal superfamily II (SF2) helicase (10, 13–17). Like the majority of Cas3 proteins, the *cas3* gene in type I-F systems encodes both the HD-nuclease and SF2-helicase domains, but unlike all other Cas3 proteins, the type I-F Cas3 is fused to a Cas2-like domain (Fig. 1*A*) (7, 18–20). Cas2 proteins play a critical role in CRISPR adaptation (i.e., the integration of foreign DNA into CRISPR loci) (21–25), and fusion of the Cas2 adaptation protein to the Cas3 interference protein suggests a functional connection between the two stages of CRISPR immunity. In fact, recent work by Vorontsova et al. has shown that new sequence acquisition (both naïve and primed) in type I-F systems requires all of the Cas proteins, including those that were previously thought to be involved exclusively in interference (26).

To determine the functional significance of the Cas2/3 fusion, we use biochemical and structural methods to show that two molecules of Cas2/3 assemble with four molecules of Cas1 ($Cas2/3_2$:$Cas1_4$) into a propeller-shaped structure and that Cas1 is a repressor of Cas2/3 nuclease activity. Collectively, this work provides the structure of a Cas1–2/3 complex and explains how Cas1 and the target-bound Csy complex are opposing regulators of Cas2/3 nuclease activity.

Results

Cas2/3 and Cas1 Form a Complex. Cas proteins Cas1 and Cas2 are necessary for the recognition and integration of new spacers into the CRISPR locus (21–23, 25, 27–29). Previous structural studies of Cas1 and Cas2 proteins from *Escherichia coli* (type I-E) have shown that four molecules of Cas1 and two molecules of Cas2 assemble into an integration complex (22–24). However, unlike other type I systems, the type I-F Cas2 adaptation protein and Cas3 interference protein are fused into a single polypeptide (7) (Fig. 1*A*). To determine if this Cas2/3 fusion protein interacts with Cas1 in the type I-F system in *Pseudomonas aeruginosa*, we

Significance

Prokaryotes have adaptive immune systems that rely on CRISPRs (clustered regularly interspaced short palindromic repeats) and diverse CRISPR-associated (*cas*) genes. Cas1 and Cas2 are conserved components of CRISPR systems that are essential for integrating fragments of foreign DNA into CRISPR loci. In type I-F immune systems, the Cas2 adaptation protein is fused to the Cas3 interference protein. Here we show that the Cas2/3 fusion protein from *Pseudomonas aeruginosa* stably associates with the Cas1 adaptation protein, forming a 375-kDa propeller-shaped Cas1–2/3 complex. We show that Cas1, in addition to being an essential adaptation protein, also functions as a repressor of Cas2/3 nuclease activity and that foreign DNA binding by the CRISPR RNA-guided surveillance complex activates the Cas2/3 nuclease.

Author contributions: M.F.R., S.C., and B.W. designed research; M.F.R., S.C., J.C., S.M.G., R.A.W., and B.W. performed research; M.F.R., S.C., J.C., S.M.G., J.B.-D., G.C.L., and B.W. analyzed data; and M.F.R., G.C.L., and B.W. wrote the paper.

The authors declare no conflict of interest.

This article is a PNAS Direct Submission.

Freely available online through the PNAS open access option.

Data deposition: The electron microscopy density maps for the Cas1–2/3 complex have been deposited at the Electron Microscopy Data Bank, http://www.ebi.ac.uk/pdbe/ (accession no. 8558).

[1]To whom correspondence should be addressed. Email: bwiedenheft@gmail.com.

This article contains supporting information online at www.pnas.org/lookup/suppl/doi:10.1073/pnas.1616395114/-/DCSupplemental.

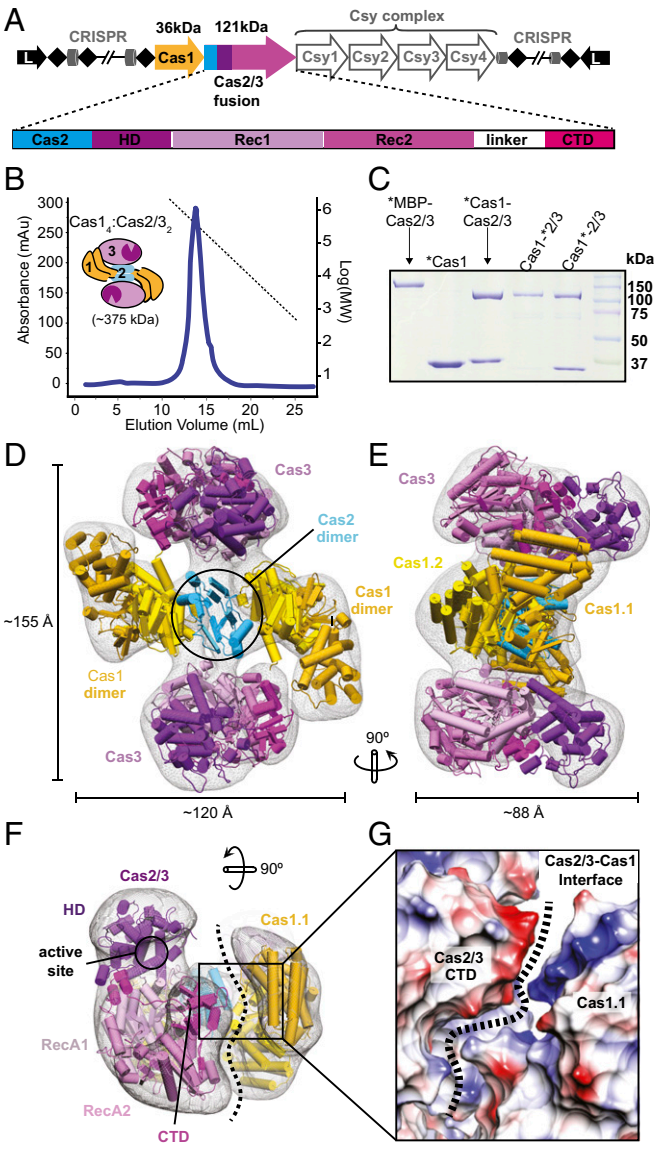

Fig. 1. Cas1 and Cas2/3 assemble into a propeller-shaped complex. (*A*) Schematic representation of the CRISPR loci and *cas* genes in the type I-F CRISPR system from *P. aeruginosa* (PA14). Two CRISPR loci composed of repeats (diamonds) and spacers (cylinders) flank six *cas* genes (arrows). In I-F systems, Cas2 (cyan) is fused to the amino terminus of Cas3. Cas3 contains an HD nuclease (purple) and two RecA domains that are connected to a CTD (pink) via a flexible linker. The theoretical molecular weights for Cas1 (36 kDa) and Cas2/3 (121 kDa) are indicated above their respective arrows. (*B*) Size-exclusion chromatography (SEC) of copurified *P. aeruginosa* proteins Cas1 and Cas2/3 reveals a stable complex with an approximate molecular weight of 375 kDa, consistent with a stoichiometry of four Cas1 subunits and two Cas2/3 proteins (i.e., Cas1$_4$:Cas2/3$_2$; theoretical MW of 386 kDa). Molecular weight standards (BioRad) were used to generate a linear regression ($R^2 = 0.98$). (*C*) Coomassie-blue stained SDS/PAGE gel. An asterisk (*) left of the protein name indicates an N-terminal tag, whereas an asterisk to the right of the protein name indicates a C-terminal tag. (*D* and *E*) Negative stain EM reconstruction of Cas1–2/3 complex (EMD 8558). A pseudoatomic model was generated by docking crystal structures of Cas1 (PDB ID code 3GOD) and Cas2/3 (PDB ID code 5B7I) into the EM density using Chimera (CC = 0.9). Proteins are colored according to the schematic in *A*. (*F*) A 90-degree rotation of the Cas1–2/3 complex reveals the unobstructed face of Cas3 and the interface with Cas1. (*G*) Charge and shape complementation along the boundary between Cas1 and the CTD of Cas2/3.

coexpressed and affinity-purified the two proteins. An amino-terminal affinity tag on Cas1 pulls down untagged Cas2/3 and the two proteins form a stable complex that elutes from a size exclusion column as a monodispersed peak with an estimated molecular weight of ~375 kDa (Fig. 1*B*). This size is consistent with a stoichiometry of four Cas1 proteins and two Cas2/3 proteins (Cas1$_4$:Cas2/3$_2$). The association between Cas1 and Cas2/3 was maintained when the affinity tag was moved to the carboxy-terminus of Cas1, whereas an amino-terminal tag on Cas2/3 abolished the interaction (Fig. 1*C*). These results are consistent with pull-down experiments performed in the type I-F CRISPR-Cas system of *Pectobacterium atrosepticum* (20) and suggest that Cas1 interacts with the amino-terminal Cas2-like domain of the Cas2/3 fusion protein (22–24).

To deduce the spatial arrangement of Cas1 and Cas2/3 within the complex, we used electron microscopy to determine the structure of the complex at ~15 Å resolution (Fig. 1*D* and Fig. S1). Overall, the structure reveals a four-lobed propeller-shaped complex, with a volume consistent with the stoichiometry predicted by our SEC analysis. A pseudoatomic model of the complex was generated by docking crystal structures of two Cas1 homodimers (30) and two Cas2/3 monomers (18) into the density (correlation coefficient, 0.91). The docking experiments reveal a central Cas2 dimer connecting two Cas1 lobes and two Cas3 lobes (Fig. 1 *D* and *E*). The core Cas2 dimer binds opposing Cas1 homodimers in an arrangement similar to the Cas1–Cas2 integration complex from *E. coli* (I-E) (22), whereas the two Cas3 proteins are positioned on opposite sides of the Cas1–2 complex in an orientation that does not occlude the protospacer DNA binding surface on Cas1-2 (Fig. 1*D* and Fig. S2*A*), nor does this interaction block the HD-nuclease or DNA binding surface on the Cas3 proteins (Fig. 1*F* and Fig. S2*C*).

The Cas3 proteins are positioned around the perimeter of the Cas1–2/3 complex, a position that is stabilized by shape and charge complementation (Fig. 1 *F* and *G*). The Cas2 domain of the Cas2/3 fusion protein interacts with the RecA1 domain of the Cas3 helicase, whereas the C-terminal domain (CTD) of Cas3 complements both shape and charge on the helical domain of Cas1. The CTD has been implicated in DNA binding and target degradation, and this interaction suggests that Cas1 may influence Cas3 function.

Cas1 and the Csy Complex Regulate Cas2/3 Nuclease Activity. In type I CRISPR systems, the crRNA-guided surveillance complex initiates DNA targeting by binding a short sequence called a Protospacer Adjacent Motif (PAM) (31, 32). PAM recognition facilitates crRNA-guided strand invasion, allowing the guide sequence of the crRNA to hybridize to the complementary strand of the foreign DNA. Target binding induces a conformational change in the complex that displaces the noncomplementary strand of DNA, resulting in an R-loop structure (33–36). The Cas3 nuclease–helicase is then recruited to degrade this displaced strand (11–13, 37, 38). Purified Cas3 from type I-E systems has been shown to unwind DNA and cleave ssDNA substrates, and recent biochemical assays performed using the *P. aeruginosa* Cas2/3 fusion protein reveal similar nuclease activity on ssDNA substrates (18). However, the impact of a Cas2 fusion on the amino terminus of Cas3, as observed in type I-F systems, or the consequence of Cas1 binding to the Cas2/3 protein has not been determined using R-loop substrates. To test the endonuclease activity of the Cas2/3 fusion protein from *P. aeruginosa*, we performed a series of degradation assays using purified Cas2/3 alone or Cas2/3 in complex with Cas1. To purify Cas2/3 in the absence of Cas1, we added maltose-binding protein (MBP) to the amino terminus to improve solubility, whereas the Cas1–2/3 complex was sufficiently soluble for purification without using a solubilization tag. Like the type I-E Cas3 proteins, the purified type I-F Cas2/3 fusion protein is unable to efficiently cleave duplexed DNA substrates (Fig. S3), but dsDNA substrates containing an internal bubble designed to mimic an R-loop are nicked within the bubble and then processively degraded (Fig. 2*A*). These results indicate that the Cas2 domain alone does not perturb canonical nuclease and helicase activities of Cas3.

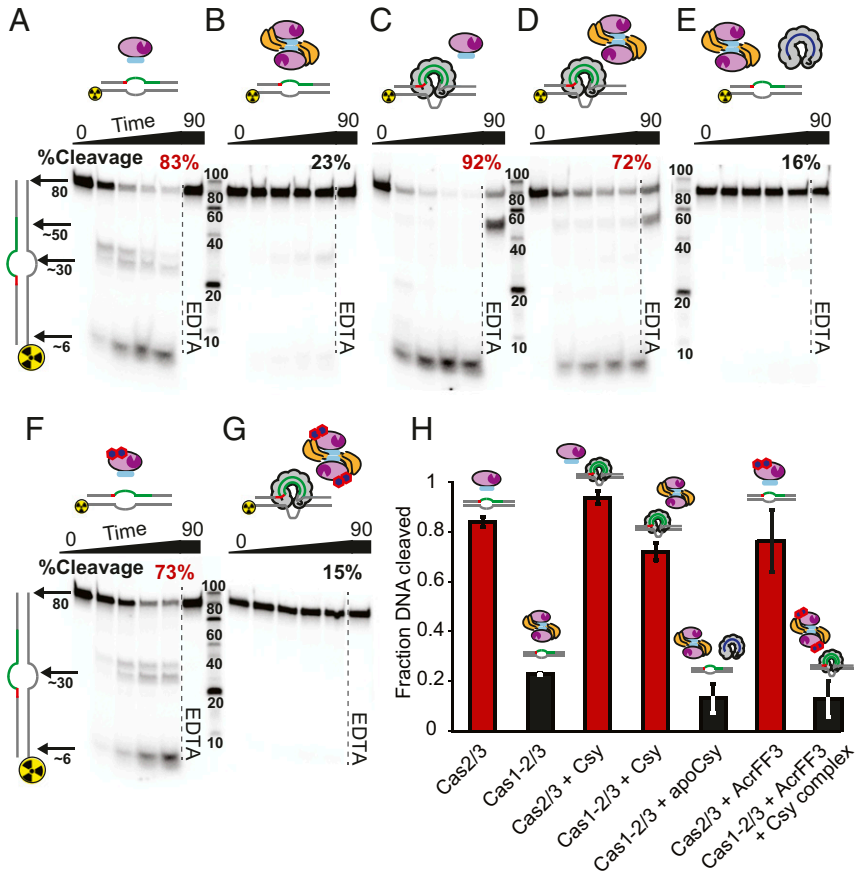

Fig. 2. Cas1 and target-bound Csy complex are opposing regulators of Cas2/3 nuclease activity. (*A*–*G*) Purified proteins (indicated in the schematic above each gel) were incubated at 37 °C with [^{32}P]-labeled dsDNA substrates containing an internal bubble. The universal symbol for ionizing radiation is used to indicate the location of the [^{32}P] label. Reactions were collected at multiple time points (0, 10, 30, 60, and 90 min) and analyzed for DNA cleavage by denaturing polyacrylamide gel electrophoresis (PAGE). The last two lanes in each gel are 90-min incubations, but the final lane also includes EDTA, which is intended to quench metal-dependent nuclease activity. The fraction of DNA cleaved is reported for the terminal time point (90 min). (*A*) Cas2/3 cleaves DNA substrates designed to mimic the R-loop generated by crRNA-guided strand invasion of dsDNA targets. (*B*) Cas1 inhibits Cas2/3 nuclease activity. (*C*) Cas2/3 cleaves DNA bound by the Csy complex. (*D*) DNA-bound Csy complex activates Cas1–2/3 nuclease activity. (*E*) Csy complex containing a crRNA (blue) that is not complementary to the target does not activate Cas1–2/3 DNA cleavage. (*F*) Anti-CRISPR protein AcrF3 does not block Cas2/3 nuclease activity. (*G*) Cas1–2/3 complex bound by AcrF3 is unable to cleave Csy-bound DNA. (*H*) Quantification of DNA cleavage at 90 min. Red and black bars are used to highlight conditions that result in high or low nuclease activity, respectively. Error bars represent SD of three replicates.

However, the same experiment performed with the Cas1–2/3 complex shows dramatically reduced DNA cleavage, suggesting that Cas1 inhibits Cas2/3 nuclease activity (Fig. 2*B*). Because nuclease activity is required for CRISPR immunity, we hypothesized that the type I-F crRNA-guided surveillance complex (Csy complex) would relieve Cas1-mediated repression of the Cas2/3 nuclease. To test this hypothesis, we purified two different Csy complexes: one containing a crRNA guide complementary to the dsDNA target, and a second containing a noncomplementary crRNA guide (Fig. 2 *D* and *E*, respectively). These two Csy complexes were incubated with DNA, and then Cas1–2/3 was added to determine if the unbound Csy complex could activate the Cas2/3 nuclease in *trans* or if crRNA-guided DNA binding is necessary for Cas2/3 activation. The results reveal that target binding is necessary for activating the Cas2/3 nuclease (Fig. 2 *D* and *E*). Together, these data suggest that Cas1 and the Csy complex are opposing regulators of Cas2/3 nuclease activity (Fig. 2*H*).

In addition to the opposing regulatory roles of Cas1 (repressor) and target-bound Csy complex (activator) in Cas2/3 nuclease activity, we also observed differences in cleavage products depending on the reaction conditions. In the absence of the Csy complex, there is no "guide" to direct the Cas2/3 nuclease to a specific location within the bubble (Fig. 2 *A* and *F*). In this case, we observe two intermediate cleavage products on the labeled strand of the ssDNA. The first 10 nucleotides of the 32-nt protospacer are noncomplementary (i.e., bubble), and we anticipate the two cleavage sites are a reflection of imprecise positioning of the HD-active site to the ssDNA bubble. In contrast, when we add Csy complex to a reaction that contains the Cas2/3 nuclease, we see little or no nicking intermediate, which suggests that Csy-mediated loading of the Cas2/3 nuclease results in rapid degradation from within the R-loop to the end of the substrate (Fig. 2 *C* and *D*). Although EDTA has been shown to be a potent inhibitor of Cas3-mediated nuclease activity in type I-E systems (15–17), we noticed a prominent nick at about position 50 on the noncomplementary strand, which is near the 3′-end of the protospacer, farthest away from the PAM (Fig. 2 *C* and *D*). Nicking at this position is most evident in reactions that contain DNA-bound Csy, EDTA, and Cas2/3 or Cas1–2/3, but a faint nicking product at this location is also detectable in the lanes without EDTA. These data suggest that either (*i*) Cas2/3 nicks at the far end of the R-loop and that addition of EDTA prevents processive degradation, resulting in a prominent band, or (*ii*) the Csy complex possesses intrinsic nuclease activity. To determine the source of the nicking activity, we performed time-course experiments with dsDNA-bound Csy without EDTA, dsDNA-bound Csy with EDTA, and dsDNA-bound

Csy with EDTA and Cas2/3 (Fig. S3). No nuclease activity is observed at any time point in the DNA-bound Csy experiments, with or without EDTA. However, nicking at the PAM distal end of the noncomplementary strand of the protospacer increases over time when DNA-bound Csy is incubated with EDTA and Cas2/3 (Fig. S3). This suggests that the Cas2/3 HD-active site maintains nicking activity in the presence of EDTA. To determine if the HD-active site is responsible for EDTA-resistant nicking, we made five different mutations in the HD-active site (i.e., H123A, H124A, H149A, H220, and H221A), one of which was soluble (i.e., H123A) (Fig. S3). Unlike wild-type Cas2/3, when we add Cas2/3 H123A to a reaction containing a DNA-bound Csy complex, we observe no nicking and no processive degradation (Fig. S3). Together, these data indicate that Cas2/3 nicking, but not processive degradation, is resistant to EDTA.

DNA degradation by Cas2/3 is essential for crRNA-guided protection from viral infection, and viruses have evolved suppressors that inhibit the CRISPR immune response (39–42). One of these suppressors, anti-CRISPR protein 3 (AcrF3), binds to Cas2/3 (18, 19, 39–43). Biochemical data and recent structural models indicate that AcrF3 blocks Cas2/3 recruitment to the target-bound Csy complex, but the impact of this interaction on Cas2/3 cleavage of R-loops has not been tested. To determine if AcrF3 binding inhibits the Cas2/3 nuclease, we purified the Cas2/3–AcrF3 complex and incubated it with the dsDNA bubble substrate (Fig. 2*F*). The results indicate that AcrF3 does not prevent DNA cleavage (Fig. S3). However, when AcrF3 is bound to the Cas1–2/3 complex, Cas2/3 could no longer be activated by target-bound Csy complex (Fig. 2*G*). Together these results suggest that AcrF3 does not directly prevent Cas2/3 nuclease activity and that the mechanism of CRISPR-mediated suppression requires blocking Cas2/3 recruitment to the target-bound Csy complex. In addition, we show that AcrF3 is capable of binding to both Cas2/3 alone and Cas1–2/3, which suggests that AcrF3 binding does not interfere with Cas1-mediated repression of Cas2/3 nuclease activity (Figs. S2*D*, S3, and S4). In fact, docking the recently published structure of AcrF3 bound to Cas2/3 into the EM density of the Cas1–2/3 complex reveals discrete binding sites for Cas1 and AcrF3 (Fig. S2*E*). This model may explain how AcrF3 blocks both target interference and new sequence adaptation (26).

DNA-Bound Csy Complex Recruits Cas2/3. Because Cas1 represses Cas2/3 nuclease activity and target-bound Csy complex restores this function, we hypothesized that Cas2/3 activation would require dissociation of the Cas1–2/3 complex. To test this hypothesis, we performed electrophoretic mobility shift assays (EMSAs) to monitor Cas2/3 recruitment to the Csy complex. As previously shown, Csy binds dsDNA targets containing a PAM and a complementary protospacer (32). Addition of Cas2/3 to the target-bound Csy complex results in a supershift (Fig. 3*A*), indicating

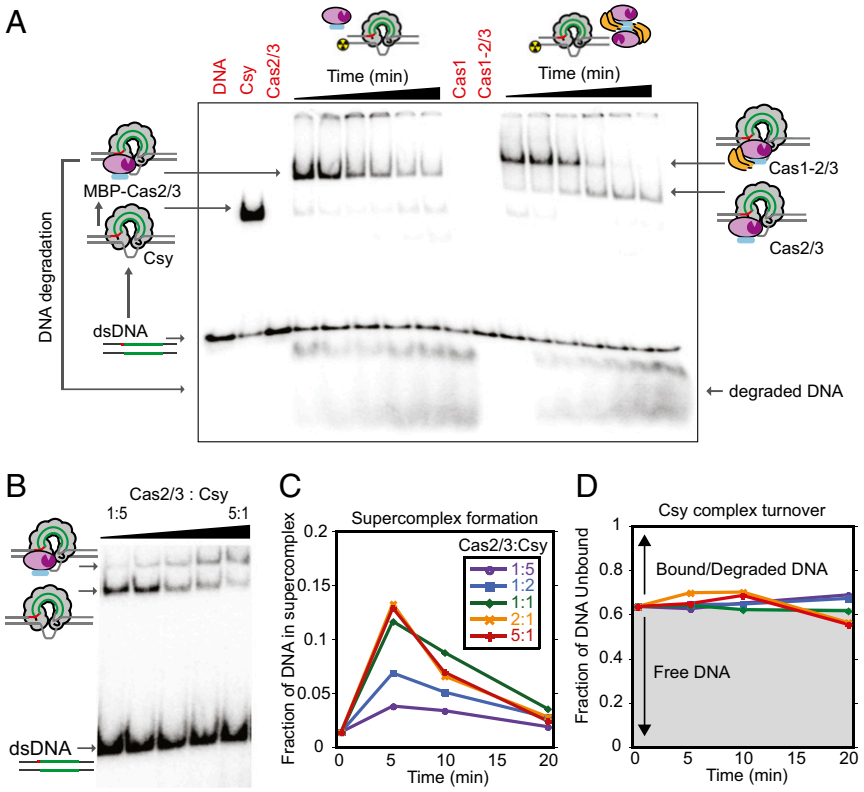

Fig. 3. Target-bound Csy complex recruits Cas1–2/3 and activates the Cas2/3 nuclease for target degradation. (*A*) EMSA performed with [^{32}P]-labeled dsDNA oligonucleotides. Lane 1 is dsDNA alone. DNA binding by Csy complex results in a pronounced shift of the target DNA. Addition of MBP-tagged Cas2/3 results in an additional shift (supershift), indicating the formation of a Cas2/3–DNA–Csy supercomplex. The intensity of the supershifted band (i.e., Cas2/3–DNA–Csy) decreases over the time course sampled (2, 5, 10, 30, 60, and 90 min), whereas the intensity of degraded DNA increases. Neither Cas1 alone nor Cas1–2/3 complex show binding or degradation of dsDNA in the absence of the Csy complex. However, addition of Cas1–2/3 to target-bound Csy results in two supershifted species; the bottom band is consistent with a Cas2/3–DNA–Csy supercomplex lacking the 40 kDa MBP fusion used to purify free Cas2/3. The upper band is most consistent with a supercomplex that includes Cas1–2/3. (*B*) EMSA performed using only enough Csy complex to bind ∼40% of the labeled DNA. Cas2/3 was added in increasing concentrations, resulting in an increase in supercomplex formation. This experiment was repeated at three time points (5, 10, and 20 min), and results were quantified. (*C*) Formation of the Csy–DNA–Cas2/3 complex increases with Cas2/3 concentration up to 1:1 Cas2/3:Csy. Additional Cas2/3 does not produce more supercomplex. (*D*) The amount of unbound DNA (∼60%) remains constant over the time course, suggesting that the Csy complex is single-turnover.

the formation of a trimeric complex composed of Csy, target DNA, and Cas2/3. Formation of the trimeric supercomplex coincides with the accumulation of Cas2/3-mediated DNA cleavage products. When we repeated these experiments with the Cas1–2/3 complex in place of Cas2/3 alone, we observed two supershifted bands. The top band migrates slower than the supercomplex formed by free Cas2/3 with target-bound Csy, and the bottom band migrates faster. The lower band is consistent with the formation of the trimeric Csy–DNA–Cas2/3 supercomplex. It is smaller than the Csy–DNA–Cas2/3 supercomplex formed when we use purified Cas2/3, but the size difference is consistent with the absence of the 40 kDa MBP fusion, which is necessary to purify Cas2/3 in the absence of Cas1. The relative position of the upper band in the Cas1–2/3 shifts is most consistent with a supercomplex that includes Csy, DNA, Cas2/3, and Cas1, although direct identification and stoichiometry of subunits in this band will require further investigation.

To monitor formation of the Csy–dsDNA–Cas2/3 supercomplex and the rate of DNA degradation, we conducted gel shift assays in which ~40% of the available dsDNA target is bound by Csy (Fig. 3*B* and Fig. S5). Cas2/3 was added in increasing concentrations, resulting in an increase in the intensity of the Csy–DNA–Cas2/3 supershift. We sampled the reactions over time and quantified supercomplex formation, degraded DNA, and the unbound dsDNA target. The results indicate that formation of the Csy–DNA–Cas2/3 complex increases with increasing Cas2/3 concentrations, up to a 1–1 stoichiometry of Cas2/3 to Csy, whereas additional Cas2/3 does not produce more of the trimeric supercomplex (Fig. 3*C*). This result is consistent with a stoichiometry of Csy_1+DNA_1+$Cas2/3_1$, which suggests that the target-bound Csy complex does not stably associate with more than one Cas2/3 (Fig. 3*C*). Additionally, highest levels of the trimeric supercomplex were detected at the earliest time point (5 min), and then the signal for the supercomplex decreased sharply. As the supercomplex dissociates, degraded DNA accumulates, but DNA in the unbound pool remains steady over the time course for all Cas2/3 concentrations (Fig. 3*D*). This result suggests that target degradation by Cas2/3 does not liberate Csy for another round of target binding, similar to the single-turnover enzyme activity reported for both Cascade (type I-E) and Cas9-mediated (type II-A) DNA cleavage (31, 44).

Cas2/3 Degrades Both Strands of DNA. crRNA-guided detection of invading DNA relies on recognition of two antigenic signatures: the PAM and the protospacer. However, strict sequence requirements present a potential weakness in the immune system because mutations in either the PAM or specific positions in the protospacer allow viruses to escape CRISPR-Cas immunity (45–47). Bacteria with type I immune systems can restore immunity against "escape" mutants by using a positive feedback loop that rapidly updates the CRISPR locus with new spacers derived from the same region of the foreign DNA that contains the mutated target (26, 46, 48–50). This process of rapid acquisition, called "primed adaptation," requires not only the adaptation proteins (i.e., Cas1 and Cas2) but also Cas3 and the crRNA-guided surveillance complex (26, 46, 51, 52). Priming in type I-F and type I-E CRISPR systems is similar, but there are important differences. In the type I-E system, the majority of new spacers acquired during priming map to the same strand as the original priming spacer (i.e., strand biased) (46, 48, 49). In contrast, priming in I-F results in new spacers derived from both strands of the target and from both sides of the priming protospacer (26, 50, 51, 53). Because Cas3 cleavage products are substrates for new sequence acquisition (52), we hypothesized that the strand-biased adaptation in I-E and the bidirectional adaptation in I-F might be explained by differences in directional degradation of the target. To test this hypothesis, we performed DNA degradation assays using dsDNA targets [^{32}P]-labeled on either the strand complementary to the crRNA guide or on the noncomplementary (displaced) strand. Purified Cas1–2/3 and Cas2/3 cleave both strands of a bound target, although the rate of cleavage is faster for the noncomplementary (displaced) strand than it is for the complementary strand (Fig. 4 *A* and *B*). Cas2/3 efficiently degrades both strands, whereas degradation assays performed using Cas1–2/3 are less efficient. When we repeated the experiment using purified Cascade and Cas3 from the *E. coli* type I-E CRISPR system, the noncomplementary strand was degraded efficiently and the differences between noncomplementary (85%) and complementary (20%) strand degradation is more pronounced than the differences between the strands in either Cas2/3 ($P = 0.003$) or Cas1–2/3 ($P = 0.006$) (Fig. 4 *A*–*C*). These results offer a mechanistic explanation for the observed difference between the two subtypes.

Discussion

CRISPR loci and their associated *cas* genes represent diverse immune systems that have been divided into a hierarchical classification consisting of 2 classes, 3 types, and 19 subtypes (7, 8). Type I systems are the most prevalent and the most diverse, representing 7 of the 19 different subtypes. Cas3 proteins are a hallmark of the type I systems, where they function as the catalytic engines of

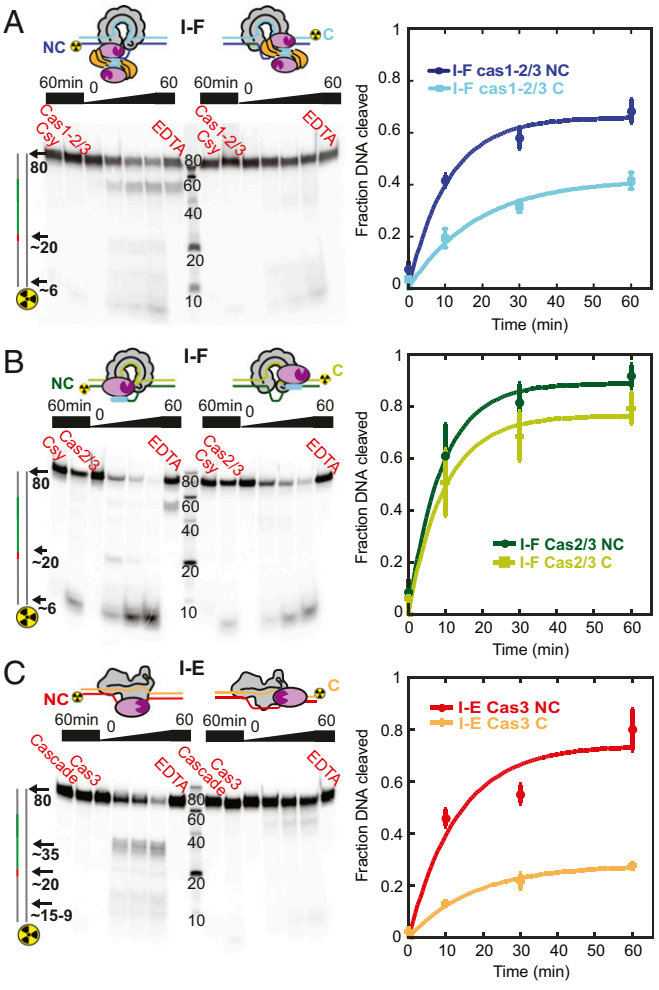

Fig. 4. Cas2/3 degrades both strands of the dsDNA target. Time course of DNA cleavage by the type I-F system (*A* and *B*) or the type I-E system (*C*). Either the complementary (C) or noncomplementary (NC) strand of a dsDNA target was [^{32}P]-labeled. Cas2/3 degrades both strands, although Cas1–2/3 is less efficient. I-E Cas3 primarily degrades the noncomplementary strand. Quantification of DNA degradation by I-F Cas2/3 and I-E Cas3 are shown next to their respective gels. Error bars represent SD of three replicates.

target degradation (14). However, recent evidence suggests that some Cas3 proteins also participate (either directly or indirectly) in new sequence acquisition (26, 51, 52). In fact, early evidence supporting this functional overlap came from bioinformatic studies that identified a unique fusion in type I-F systems that links a Cas2-like adaptation protein to the amino terminus of the Cas3 interference protein (i.e., Cas2/3) (54). Indeed, Cas1 and Cas2/3 have been shown to interact in *P. atrosepticum*, but the structural and functional implications of the Cas2/3 fusion have not been determined (20). Here we show that Cas2/3 from *P. aeruginosa* stably associates with the Cas1 adaptation protein, forming a 375-kDa propeller-shaped complex consisting of two Cas2/3 proteins and four Cas1 proteins ($Cas1_4$:$Cas2/3_2$) (Fig. 1).

The adaptation proteins Cas1 and Cas2 are conserved components of CRISPR systems, and these two proteins have been shown to be necessary for new spacer acquisition in the type I-E systems (7, 21, 55). In *E. coli*, Cas1 and Cas2 assemble into a stable integration complex, and a structure of this complex fits with high confidence into a portion of the electron density in our Cas1–2/3 reconstruction (Fig. S2*A*) (22). However, DNA binding by the integration complex introduces a rotation in the Cas1 proteins, and this DNA bound conformation no longer fits in the Cas1–2/3 density (Fig. S2*B*) (18, 23). In *E. coli*, this DNA-induced conformational change is unconstrained by additional proteins, but in type I-F systems, the large Cas3 domains (~110 kDa) are wedged between the Cas1 lobes. The DNA binding surface of the type I-F Cas1-2 integration complex is unobstructed by Cas3, but a DNA-induced rotation of Cas1 would clash with the Cas3 lobes in our reconstruction (Fig. S2*B*). This suggests that DNA binding by the Cas1–Cas2 complex in the I-F system will result in a corresponding conformational change in the Cas3 lobes. Higher resolution structures of Cas1–2/3 before and after DNA binding will be important for understanding the orchestrated rearrangement of these proteins and the functional implications of these interactions.

The first structure of Cas1 revealed a butterfly-shaped homodimer, where each subunit represented one wing of the butterfly (30). Docking high-resolution structures of *P. aeruginosa* Cas1 and Cas2/3 into the Cas1–2/3 EM density reveals shape and charge complementation between the "wing" of one Cas1 molecule in each homodimer and the CTD of each Cas3 (Fig. 1 *F* and *G*). In the I-E system, the CTD of Cas3 functions as a lid that folds over the top of the DNA binding cleft (13). A flexible hinge connects the CTD to the helicase domain and allows the lid to open while loading the Cas3 helicase onto the displaced strand of the target DNA. In the I-F Cas1–2/3 complex, the interaction between Cas1 and the CTD suggests that Cas1 stabilizes the CTD in a closed conformation that restricts DNA access to the HD-active site. Although this interaction appears to be a potent inhibitor of Cas2/3-mediated DNA cleavage (Fig. 2), it does not prevent Cas1–2/3 from recognizing a target-bound Csy complex (Figs. 2 and 3). Csy-mediated recruitment of Cas1–2/3 results in activation of the Cas2/3 nuclease (Fig. 3*A*), although we do not know if activation requires complete dissociation of all Cas1 subunits. In fact, addition of Cas1–2/3 to the target-bound Csy complex results in a supershift that is only slightly larger than the supershift we see with MBP–Cas2/3 (~160 kDa) (Fig. 3*A*). The modest increase in size suggests that the $Cas1_4$:$Cas2/3_2$ complex may dissociate into a nuclease-active complex that includes Cas1. We show that the activated nuclease initially degrades the displaced (i.e., noncomplementary) strand in the 3-to-5 prime directions (Fig. 4), and degradation products may serve as substrates for new sequence acquisition (52). Initial degradation of the noncomplementary strand is similar to Cas3-mediated degradation of DNA targets in the I-E system. However, unlike the I-E systems, where the crRNA-guided surveillance complex recruits a single Cas3 for unidirectional 3-to-5 prime degradation of the displaced strand (31), the activated Cas2/3 appears to degrade both strands of Csy-targeted DNA (Fig. 4). This degradation pattern offers a mechanistic explanation of bidirectional spacer acquisition in I-F immune systems (26, 50, 51).

What is the selective pressure that preserves the Cas2/3 fusion, and why is this fusion not maintained in other CRISPR systems? An evolutionary analysis performed by Koonin and coworkers predicted that Cas1 and Cas2 originally functioned as a toxin–antitoxin pair (56). We find this prediction intriguing, and our biochemical data, combined with recent insights about the role of Cas1 and Cas2 in CRISPR adaptation, may support a revised version of this evolutionary model. Here we show that Cas2/3 is a nuclease that will cleave DNA bubbles designed to mimic R-loops in the absence of a crRNA-guided surveillance complex (Fig. 2*A*). This suggests that any single-stranded DNA intermediate in the cell could be a substrate for spurious Cas2/3 nuclease activity. We show that Cas1 represses this activity pending specific activation by recruitment to the crRNA-guided surveillance complex bound to a target. In this regard, Cas1 may function as an antitoxin that represses toxic Cas2/3 nuclease activity. But if Cas1 is an important repressor of nonspecific nuclease activity, then why is the Cas2/3 fusion not conserved in other CRISPR systems? There are many possible explanations, and we do not claim to have an authoritative answer. However, virus-encoded anti-CRISPRs antagonize CRISPR-mediated immune systems and are expected to drive immune system diversification (41, 57, 58). Bondy-Denomy et al. showed that the anti-CRISPR protein AcrF3 binds to Cas2/3 and blocks recruitment to the Csy complex, and recently determined structures of AcrF3 bound to Cas2/3 explain how the AcrF3 proteins blocks DNA access to the RecA domains of the Cas3 helicase. However, in addition to binding Cas2/3, we show that AcrF3 binds directly to the Cas1–2/3 complex. This interaction may help explain how AcrF3 also blocks new sequence acquisition (26). An anti-CRISPR capable of neutralizing the protein complex responsible for both adaptation and interference (i.e., Cas1–2/3) may reveal an Achilles heel of the I-F system.

Materials and Methods

Protein Expression and Purification.

P. aeruginosa *Csy complex*. Csy genes and a synthetic CRISPR were coexpressed on separate vectors in *E. coli* BL21 (DE3) cells as previously described (32, 59) (AddGene ID 89232, 89244). Expression was induced with 0.5 mM isopropyl-D-1-thiogalactopyranoside (IPTG) at OD_{600} = 0.5 nm. Cells were incubated overnight at 16 °C, then pelleted by centrifugation (5,000 × *g* for 15 min at 4 °C), and resuspended in lysis buffer [50 mM 4-(2-hydroxyethyl)-1-piperazineethanesulfonic acid (Hepes) pH 7.5, 300 mM potassium chloride, 5% glycerol, 1 mM Tris(2-carboxyethyl) phosphine hydrochloride (TCEP), 1× protease inhibitor mixture (Thermo Scientific)]. Pellets were sonicated on ice for 3 × 2.5 min (1 s on, 3 s off), and then the lysate was clarified by centrifugation at 22,000 × *g* for 30 min at 4 °C. The Csy complex self-assembles in vivo, and the intact complex was affinity-purified over StrepTrap HP resin (GE) using strep-II tags on Csy3. Protein was eluted with lysis buffer supplemented with 2.5 mM desthiobiotin and then concentrated (Corning Spin-X concentrators) at 4 °C before further purification over a Superdex 200 size-exclusion column (GE Healthcare) in 20 mM Hepes pH 7.5, 100 mM KCl, 5% glycerol, and 1 mM TCEP.

P. aeruginosa *Cas2/3*. The *cas2/3* gene from *P. aeruginosa* (PA14) was cloned with an N-terminal Strep-II tag and MBP into a spectinomycin resistance (2S) LIC vector as previously described (39) (AddGene ID 89238). This plasmid was used as a template for making the N-terminal SUMO tagged Cas2/3 expression vector (AddGene ID 89239). In brief, the Strep-II tag and MBP were removed using SacI and NcoI, and the SUMO tag was PCR-amplified using primers containing SacI and NcoI resection sites (F_primer, CGACCATGGGCCGTCAGGAGTCAAGACTGA, and R_primer, CGAGAGCTCCCACCGGTCTGCTGTTGGAAC). Plasmids were transformed into *E. coli* BL21 (DE3) cells. Expression was induced with 0.5 mM IPTG at OD_{600} = 0.5 nm. Cells were pelleted and lysed as described above. Cas2/3 was affinity-purified using StrepTrap HP resin (GE), eluted with lysis buffer supplemented with 2.5 mM desthiobiotin, and then concentrated (Corning Spin-X concentrators) at 4 °C before further purification over a Superdex 200 size-exclusion column (GE Healthcare) in 20 mM Hepes pH 7.5, 150 mM KCl, and 5% glycerol. An HD nuclease (H123A) mutant was generated using the Q5 mutagenesis method (New England Biolabs) (mutagenesis primers: forward, AGCGCTGTTCGCCGATATCGGCAAGG; reverse, GCCATCACCGTCAGCAGG).

P. aeruginosa *Cas1–2/3 complex.* The *cas1* and *cas2/3* genes from *P. aeruginosa* were PCR-amplified and cloned into a spectinomycin-resistant p2S LIC vector (AddGene ID 89230). The Q5 mutagenesis method was used to generate constructs with *N*- or C-terminal 6-histidine tags on Cas1 or an N-terminal 6-histidine tag on Cas2/3. We also made a construct with an N-terminal Strep-II tag on Cas1. Plasmids were transformed into *E. coli* BL21 (DE3) cells for expression. Initial pull-down experiments were conducted with *N*- or C-terminal 6-histidine affinity tags, as indicated. Expression was induced with 0.5 mM IPTG at OD_{600} = 0.5 nm. Cells were pelleted and lysed as described above. Coexpressed Cas1 and Cas2/3 were affinity-purified using NiNTA resin (Qiagen), which was washed once with lysis buffer supplemented with 20 mM imidazole before elution with lysis buffer supplemented with 300 mM imidazole. Eluate was concentrated (Corning Spin-X concentrators) at 4 °C before evaluation by SDS/PAGE. The Cas1–2/3 complex used for electron microscopy was prepared using an N-terminal strep-II affinity tag on Cas1 and was expressed and purified as described for Cas2/3.

AcrF3. Anti-CRISPR protein AcrF3 was expressed and purified as previously described (39) (AddGene ID 89246). Expression, cell pelleting, and sonication were performed as described above. Protein was purified over NiNTA resin (Qiagen) in lysis buffer [50 mM Tris, pH 7.5, 300 mM sodium chloride, 5% glycerol, 1× protease inhibitor mixture (Thermo Scientific); wash buffer included 20 mM imidazole; elution buffer included 300 mM imidazole]. Eluted protein was concentrated (Corning Spin-X concentrators) at 4 °C before further purification over a Superdex 75 size-exclusion column (GE Healthcare) in 20 mM Tris, pH 7.5, 150 mM NaCl, and 5% glycerol.

E. coli *Cascade (I-E).* Cascade genes and a synthetic CRISPR were coexpressed on separate vectors in *E. coli* BL21 (DE3) cells as previously described (59). Expression was induced with 0.5 mM IPTG at OD_{600} = 0.5 nm. Cells were incubated overnight at 16 °C, then pelleted by centrifugation (5,000 × *g* for 15 min at 4 °C), and resuspended in lysis buffer [50 mM Hepes, pH 7.5, 300 mM potassium chloride, 5% glycerol, 1 mM TCEP, 1× protease inhibitor mixture (Thermo Scientific)]. Pellets were sonicated on ice for 3 × 2.5 min (1 s on, 3 s off), and then the lysate was clarified by centrifugation at 22,000 × *g* for 30 min at 4 °C. Cascade self-assembles in vivo, and the intact complex was affinity-purified over StrepTrap HP resin (GE) using strep-II tags on CasB. Protein was eluted with lysis buffer supplemented with 2.5 mM desthiobiotin and then concentrated (Corning Spin-X concentrators) at 4 °C before further purification over a Superdex 200 size-exclusion column (GE Healthcare) in 20 mM Hepes, pH 7.5, 100 mM KCl, 5% glycerol, and 1 mM TCEP.

E. coli *Cas3.* MBP–Cas3 was expressed and purified as previously described (11). The *cas3* gene from *E. coli* was cloned with an N-terminal Strep-II tag and a MBP. The plasmid was transformed into *E. coli* BL21 (DE3) cells. Expression was induced with 0.5 mM IPTG at OD_{600} = 0.5 nm. Cells were pelleted and lysed as described above. Strep–MBP–Cas3 was affinity-purified using StrepTrap HP resin (GE), eluted with lysis buffer supplemented with 2.5 mM desthiobiotin, and then concentrated (Corning Spin-X concentrators) at 4 °C before further purification over a Superdex 200 size-exclusion column (GE Healthcare) in 20 mM Hepes, pH 7.5, 150 mM KCl, and 10% glycerol.

Negative-Stain Electron Microscopy.

Sample preparation. We applied 3 μL of purified Cas1–2/3 complex (0.03 mg/mL) to freshly plasma-cleaned 400 mesh Cu–Rh maxtaform grids (Electron Microscopy Sciences) that were coated with a thin layer of amorphous carbon. After incubating for 1 min at room temperature, excess protein was wicked off with a filter paper (Whatman No. 1), and the grid was immediately inverted and placed on a 50 μL droplet of 2% (wt/vol) uranyl formate solution. After 30 s, excess stain was wicked off from the grid by touching the edge with filter paper. This staining step was repeated three more times for thorough embedding of the sample, and the grids were air-dried after the last blotting step.

Data acquisition. Data for all of the samples were acquired in a Tecnai Spirit (FEI) transmission electron microscope, operating at 120 keV, using the Leginon automated data acquisition system (60). Micrographs were acquired at a nominal magnification of 52,000× on an F416 CMOS 4K×4K camera (TVIPS) with a pixel size of 2.05 Å per pixel at the specimen level using an electron dose of 30 electrons per $Å^2$, with a 1-μm defocus.

Image processing. A total of 1,159 negative stained micrographs were collected (Fig. S1*A*). The Appion image processing pipeline (61) was used for processing of the micrographs. CTFFIND4 (62) was used for determining the contrast transfer function (CTF) of each micrograph, and particles were selected from micrographs using a Difference of Gaussians (DoG)-based automated particle picker (63). Phases for each micrograph were corrected using EMAN (64), and 221,700 particles were extracted using a 192 × 192 pixel box. For faster computation, the particles were binned by a factor of two to 96 × 96. Individual particles were normalized by eliminating pixels with values above or below 4.5 σ of the mean pixel value using the normalization function in Relion1.4 (65). The normalized particle stack was then subjected to reference-free 2D classification and alignment using Relion (Fig. S1*B*). We selected 138,719 particles from 163 well-aligned 2D class averages depicting different views and conformations of the complex (Fig. S1*D*). An initial 3D reference was generated with the selected class averages using sxviper program of the SPARX EM data processing package (sparx-em.org) (66). This initial reference was low pass filtered to 60 Å resolution and was used as a starting model for 25 iterations of 3D classification into eight classes. A total of 68,929 particles belonging to two similar 3D classes that represented the full Cas1–2/3 complex were combined and subjected to 3D refinement in Relion. A five-pixel extended and eight-pixel falloff-smoothed binary 3D mask was created out of the final refined volume, and further 3D refinement was continued with this binary mask until the refinement converged. Particles after masked 3D refinement were subjected to another 25 iterations of 3D classification into three classes, using the binary mask as the reference mask. A total of 26,403 particles belonging to the most structurally featureful 3D class were further subjected to 3D refinement with the binary mask. The final 3D reconstruction (Fig. 1*C*) after convergence of refinement was at a resolution of 15.6 Å (Fig. S1*C*) by Gold Standard Fourier Shell Correlation at a cutoff of 0.143. The final EM map is deposited in the EM data bank with accession no. EMD 8558. Crystal structures of *P. aeruginosa* Cas1 [Protein Data Bank (PDB) ID code 3GOD] and Cas2/3 (PDB ID code 5B7I) were docked into the final EM density map using UCSF Chimera (67). The position of the Cas2 domains was performed by first docking the *E. coli* Cas1–Cas2 structure (PDB ID code 4P6I) into the density and then superimposing each I-F Cas2 domain on corresponding subunits in the I-E Cas2 dimer. The Cas2 proteins superimpose with an average root-mean-square deviation (rmsd) of 1.75 Å for equivalently positioned C-alpha atoms.

Nuclease Activity Assay with [^{32}P]-Labeled DNA.

Nuclease activity assay with dsDNA bubble substrates. We incubated 100 nM Cas2/3 or 50 nM Cas1–2/3 complex (a single Cas1–2/3 complex contains 2 Cas2/3 monomers) with 5′ [^{32}P]-labeled 80-bp dsDNA oligonucleotides containing an internal 10-nucleotide bubble, at 37 °C in reaction buffer (20 mM Hepes, pH 7.5, 100 mM KCl, 5% glycerol, 1 mM TCEP, 5 mM $MgCl_2$, 75 μM $NiSO_4$, 5 mM $CaCl_2$, 1 mM ATP) for 0, 10, 30, 60, or 90 min. When Csy complex was included, DNA was preincubated with 200 nM Csy at 37 °C for 15 min before the addition of Cas2/3 or Cas1–2/3. When anti-CRISPR AcrF3 was included, Cas2/3 or Cas1–Cas2/3 was preincubated with 12× molar excess of AcrF3 for 15 min at 37 °C. Reactions were quenched with 1% SDS, 8 mM EDTA, and the products separated by electrophoresis over 14% polyacrylamide gels containing 7 M urea. Dried gels were imaged with a phosphor storage screen (Kodak) and then scanned with a Typhoon phosphorimager (GE Healthcare). The signal in each band was quantified using ImageQuant software.

I-F vs. I-E DNA strand cleavage assay. We incubated 100 nM Cas2/3 (I-F), Cas3 (I-E), or 50 nM Cas1–2/3 complex (I-F) with 5′ [^{32}P]-labeled dsDNA oligonucleotides (Table S1), at 37 °C in reaction buffer (20 mM Hepes pH 7.5, 100 mM KCl, 5% glycerol, 1 mM TCEP, 5 mM $MgCl_2$, 75 μM $NiSO_4$, 5 mM $CaCl_2$, and 1 mM ATP) for 0, 10, 30, or 60 min. When Csy complex (I-F) or Cascade (I-E) was included, DNA was preincubated with 200 nM Csy or Cascade at 37 °C for 15 min before the addition of Cas2/3, Cas3, or Cas1–2/3. Reactions were quenched with 1% SDS, 8 mM EDTA, and the products separated by electrophoresis over 14% polyacrylamide gels containing 7 M urea. The gels were dried, exposed to phosphor storage screens (Kodak), and then scanned with a Typhoon phosphorimager (GE Healthcare). The signal in each band was quantified using ImageQuant software. Percent degradation was plotted for each time point (error bars represent SD of the mean for three replicates), and the data were fit using a single-term exponential equation: $y = a*[1 - \exp(-k*x)]$ (KaleidaGraph Software). The difference in percent degradation for the noncomplementary and complementary strands was calculated for each experiment. Differential strand degradations by Cas2/3 and Cas1–2/3 were individually compared with Cas3 using a Student's *t* test.

EMSAs.

Cas1–2/3 recruitment assay. We incubated 100 nM Cas2/3 or 50 nM Cas1–2/3 complex with 5′ [^{32}P]-labeled 80-bp dsDNA at 37 °C in reaction buffer (20 mM Hepes, pH 7.5, 300 mM KCl, 5% glycerol, 1 mM TCEP, 5 mM $MgCl_2$, 75 μM $NiSO_4$, 5 mM $CaCl_2$, and 1 mM ATP) for 2, 5, 10, 30, 60, or 90 min. When Csy complex was included, DNA was preincubated with 150 nM Csy at 37 °C for 15 min before the addition of Cas2/3 or Cas1–2/3. Csy binding reactions were performed at 100 mM KCl, and then KCl concentration was increased to 300 mM KCl before addition of Cas2/3. Reactions were

separated by electrophoresis over native 4.5% polyacrylamide gels. Dried gels were imaged with a phosphor storage screen (Kodak) and then scanned with a Typhoon phosphorimager (GE Healthcare).

Supercomplex assay. We preincubated 5′ [^{32}P]-labeled 80-bp dsDNA with 10 nM Csy complex at 37 °C in reaction buffer for 15 min before the addition of 2 nM, 5 nM, 10 nM, 20 nM, or 50 nM Cas2/3. Experiment was repeated with 5, 10, and 20-min incubation times, with and without Cas2/3. Reactions were separated by electrophoresis over native 4.5% polyacrylamide gels. Dried gels were imaged with a phosphor storage screen (Kodak), scanned with a Typhoon phosphorimager (GE Healthcare), and band intensities were quantified using ImageQuant software. Reactions without Cas2/3 were used for background subtraction of nonspecific degradation.

AcrF3+Cas2/3 Nuclease Activity Assay with M13 ssDNA. This assay was performed as previously published (18). We incubated 5 nM M13mp18 ssDNA (New England Biolabs, cat. no. N4040S) at 37 °C with 200 nM Cas2/3 in reaction buffer containing 10 mM Tris·HCl, pH 7.5, 100 mM KCl, 1% glycerol, 2 mM $MnCl_2$, 2 mM $NiSO_4$, and 2 mM $CaCl_2$. Anti-CRISPR AcrF3 was included in reactions at 2 μM and was prebound to Cas2/3 for 2 h at 4 °C. Reactions were sampled at 0.5, 1, and 2.5 h before separation on a 0.8% agarose gel.

ACKNOWLEDGMENTS. We thank members of the B.W. laboratory for critical feedback and thoughtful discussion regarding this manuscript. We thank the anonymous referees for pointing out the nicking product in our EDTA control lanes. G.C.L. is supported as a Searle Scholar, a Pew Scholar, and by National Institutes of Health Grant DP2EB020402. J.B.-D. is supported by the University of California San Francisco Program for Breakthrough in Biomedical Research, funded in part by the Sandler Foundation, and NIH Office of the Director Early Independence Award DP5-OD021344. Research in the B.W. laboratory is supported by National Institutes of Health Grants P20GM103500, P30GM110732-03, R01GM110270, and R01GM108888; National Science Foundation EPSCoR Grant EPS-110134, the M. J. Murdock Charitable Trust, a young investigator award from Amgen, and the Montana State University Agricultural Experimental Station.

1. Mohanraju P, et al. (2016) Diverse evolutionary roots and mechanistic variations of the CRISPR-Cas systems. *Science* 353:aad5147.
2. Marraffini LA (2015) CRISPR-Cas immunity in prokaryotes. *Nature* 526:55–61.
3. Carter J, Wiedenheft B (2015) SnapShot: CRISPR-RNA-guided adaptive immune systems. *Cell* 163:260–260 e261.
4. Sternberg SH, Richter H, Charpentier E, Qimron U (2016) Adaptation in CRISPR-Cas systems. *Mol Cell* 61:797–808.
5. Amitai G, Sorek R (2016) CRISPR-Cas adaptation: Insights into the mechanism of action. *Nat Rev Microbiol* 14:67–76.
6. Jackson RN, Wiedenheft B (2015) A conserved structural chassis for mounting versatile CRISPR RNA-guided immune responses. *Mol Cell* 58:722–728.
7. Makarova KS, et al. (2015) An updated evolutionary classification of CRISPR-Cas systems. *Nat Rev Microbiol* 13:722–736.
8. Shmakov S, et al. (2015) Discovery and functional characterization of diverse class 2 CRISPR-Cas systems. *Mol Cell* 60:385–397.
9. Westra ER, et al. (2012) Cascade-mediated binding and bending of negatively supercoiled DNA. *RNA Biol* 9:1134–1138.
10. Gong B, et al. (2014) Molecular insights into DNA interference by CRISPR-associated nuclease-helicase Cas3. *Proc Natl Acad Sci USA* 111:16359–16364.
11. Mulepati S, Bailey S (2013) In vitro reconstitution of an Escherichia coli RNA-guided immune system reveals unidirectional, ATP-dependent degradation of DNA target. *J Biol Chem* 288:22184–22192.
12. Sinkunas T, et al. (2013) In vitro reconstitution of Cascade-mediated CRISPR immunity in Streptococcus thermophilus. *EMBO J* 32:385–394.
13. Huo Y, et al. (2014) Structures of CRISPR Cas3 offer mechanistic insights into Cascade-activated DNA unwinding and degradation. *Nat Struct Mol Biol* 21:771–777.
14. Jackson RN, Lavin M, Carter J, Wiedenheft B (2014) Fitting CRISPR-associated Cas3 into the helicase family tree. *Curr Opin Struct Biol* 24:106–114.
15. Beloglazova N, et al. (2011) Structure and activity of the Cas3 HD nuclease MJ0384, an effector enzyme of the CRISPR interference. *EMBO J* 30:4616–4627.
16. Mulepati S, Bailey S (2011) Structural and biochemical analysis of nuclease domain of clustered regularly interspaced short palindromic repeat (CRISPR)-associated protein 3 (Cas3). *J Biol Chem* 286:31896–31903.
17. Sinkunas T, et al. (2011) Cas3 is a single-stranded DNA nuclease and ATP-dependent helicase in the CRISPR/Cas immune system. *EMBO J* 30:1335–1342.
18. Wang X, et al. (2016) Structural basis of Cas3 inhibition by the bacteriophage protein AcrF3. *Nat Struct Mol Biol* 23:868–870.
19. Wang J, et al. (2016) A CRISPR evolutionary arms race: Structural insights into viral anti-CRISPR/Cas responses. *Cell Res* 26:1165–1168.
20. Richter C, Gristwood T, Clulow JS, Fineran PC (2012) In vivo protein interactions and complex formation in the Pectobacterium atrosepticum subtype I-F CRISPR/Cas system. *PLoS One* 7:e49549.
21. Yosef I, Goren MG, Qimron U (2012) Proteins and DNA elements essential for the CRISPR adaptation process in Escherichia coli. *Nucleic Acids Res* 40:5569–5576.
22. Nuñez JK, et al. (2014) Cas1-Cas2 complex formation mediates spacer acquisition during CRISPR-Cas adaptive immunity. *Nat Struct Mol Biol* 21:528–534.
23. Nuñez JK, Harrington LB, Kranzusch PJ, Engelman AN, Doudna JA (2015) Foreign DNA capture during CRISPR-Cas adaptive immunity. *Nature* 527:535–538.
24. Wang J, et al. (2015) Structural and mechanistic basis of PAM-dependent spacer acquisition in CRISPR-Cas systems. *Cell* 163:840–853.
25. Arslan Z, Hermanns V, Wurm R, Wagner R, Pul Ü (2014) Detection and characterization of spacer integration intermediates in type I-E CRISPR-Cas system. *Nucleic Acids Res* 42:7884–7893.
26. Vorontsova D, et al. (2015) Foreign DNA acquisition by the I-F CRISPR-Cas system requires all components of the interference machinery. *Nucleic Acids Res* 43:10848–10860.
27. Rollie C, Schneider S, Brinkmann AS, Bolt EL, White MF (2015) Intrinsic sequence specificity of the Cas1 integrase directs new spacer acquisition. *eLife* 4:4.
28. Nuñez JK, Lee AS, Engelman A, Doudna JA (2015) Integrase-mediated spacer acquisition during CRISPR-Cas adaptive immunity. *Nature* 519:193–198.
29. Wright AV, Doudna JA (2016) Protecting genome integrity during CRISPR immune adaptation. *Nat Struct Mol Biol* 23:876–883.
30. Wiedenheft B, et al. (2009) Structural basis for DNase activity of a conserved protein implicated in CRISPR-mediated genome defense. *Structure* 17:904–912.
31. Redding S, et al. (2015) Surveillance and processing of foreign DNA by the Escherichia coli CRISPR-Cas system. *Cell* 163:854–865.
32. Rollins MF, Schuman JT, Paulus K, Bukhari HS, Wiedenheft B (2015) Mechanism of foreign DNA recognition by a CRISPR RNA-guided surveillance complex from Pseudomonas aeruginosa. *Nucleic Acids Res* 43:2216–2222.
33. Szczelkun MD, et al. (2014) Direct observation of R-loop formation by single RNA-guided Cas9 and Cascade effector complexes. *Proc Natl Acad Sci USA* 111:9798–9803.
34. Rutkauskas M, et al. (2015) Directional R-loop formation by the CRISPR-Cas surveillance complex cascade provides efficient off-target site rejection. *Cell Reports* S2211-1247(15)00135-7.
35. Blosser TR, et al. (2015) Two distinct DNA binding modes guide dual roles of a CRISPR-Cas protein complex. *Mol Cell* 58:60–70.
36. Hayes RP, et al. (2016) Structural basis for promiscuous PAM recognition in type I-E Cascade from E. coli. *Nature* 530:499–503.
37. Hochstrasser ML, et al. (2014) CasA mediates Cas3-catalyzed target degradation during CRISPR RNA-guided interference. *Proc Natl Acad Sci USA* 111:6618–6623.
38. Westra ER, et al. (2012) CRISPR immunity relies on the consecutive binding and degradation of negatively supercoiled invader DNA by Cascade and Cas3. *Mol Cell* 46:595–605.
39. Bondy-Denomy J, et al. (2015) Multiple mechanisms for CRISPR-Cas inhibition by anti-CRISPR proteins. *Nature* 526:136–139.
40. Bondy-Denomy J, Pawluk A, Maxwell KL, Davidson AR (2013) Bacteriophage genes that inactivate the CRISPR/Cas bacterial immune system. *Nature* 493:429–432.
41. Pawluk A, et al. (2016) Inactivation of CRISPR-Cas systems by anti-CRISPR proteins in diverse bacterial species. *Nat Microbiol* 1:16085.
42. Chowdhury S, et al. (2017) Structure reveals mechanisms of viral suppressors that intercept a CRISPR RNA-guided surveillance complex. *Cell* 169:47–57.
43. Mallon J, Bailey S (2016) A molecular arms race: New insights into anti-CRISPR mechanisms. *Nat Struct Mol Biol* 23:765–766.
44. Sternberg SH, Redding S, Jinek M, Greene EC, Doudna JA (2014) DNA interrogation by the CRISPR RNA-guided endonuclease Cas9. *Nature* 507:62–67.
45. Cady KC, Bondy-Denomy J, Heussler GE, Davidson AR, O'Toole GA (2012) The CRISPR/Cas adaptive immune system of Pseudomonas aeruginosa mediates resistance to naturally occurring and engineered phages. *J Bacteriol* 194:5728–5738.
46. Datsenko KA, et al. (2012) Molecular memory of prior infections activates the CRISPR/Cas adaptive bacterial immunity system. *Nat Commun* 3:945.
47. Semenova E, et al. (2011) Interference by clustered regularly interspaced short palindromic repeat (CRISPR) RNA is governed by a seed sequence. *Proc Natl Acad Sci USA* 108:10098–10103.
48. Fineran PC, et al. (2014) Degenerate target sites mediate rapid primed CRISPR adaptation. *Proc Natl Acad Sci USA* 111:E1629–E1638.
49. Swarts DC, Mosterd C, van Passel MW, Brouns SJ (2012) CRISPR interference directs strand specific spacer acquisition. *PLoS One* 7:e35888.
50. Richter C, et al. (2014) Priming in the Type I-F CRISPR-Cas system triggers strand-independent spacer acquisition, bi-directionally from the primed protospacer. *Nucleic Acids Res* 42:8516–8526.
51. Staals RH, et al. (2016) Interference-driven spacer acquisition is dominant over naive and primed adaptation in a native CRISPR-Cas system. *Nat Commun* 7:12853.
52. Künne T, et al. (2016) Cas3-derived target DNA degradation fragments fuel primed CRISPR adaptation. *Mol Cell* 63:852–864.
53. Heussler GE, Miller JL, Price CE, Collins AJ, O'Toole GA (2016) Requirements for Pseudomonas aeruginosa Type I-F CRISPR-Cas adaptation determined using a biofilm enrichment assay. *J Bacteriol* 198:3080–3090.
54. Makarova KS, Grishin NV, Shabalina SA, Wolf YI, Koonin EV (2006) A putative RNA-interference-based immune system in prokaryotes: Computational analysis of the predicted enzymatic machinery, functional analogies with eukaryotic RNAi, and hypothetical mechanisms of action. *Biol Direct* 1:7.
55. Ivančić-Baće I, Cass SD, Wearne SJ, Bolt EL (2015) Different genome stability proteins underpin primed and naïve adaptation in E. coli CRISPR-Cas immunity. *Nucleic Acids Res* 43:10821–10830.

56. Makarova KS, Wolf YI, Koonin EV (2013) Comparative genomics of defense systems in archaea and bacteria. *Nucleic Acids Res* 41:4360–4377.
57. Wiedenheft B (2013) In defense of phage: Viral suppressors of CRISPR-mediated adaptive immunity in bacteria. *RNA Biol* 10:886–890.
58. Briner AE, Barrangou R (2016) Deciphering and shaping bacterial diversity through CRISPR. *Curr Opin Microbiol* 31:101–108.
59. Wiedenheft B, et al. (2011) RNA-guided complex from a bacterial immune system enhances target recognition through seed sequence interactions. *Proc Natl Acad Sci USA* 108:10092–10097.
60. Suloway C, et al. (2005) Automated molecular microscopy: The new Leginon system. *J Struct Biol* 151:41–60.
61. Lander GC, et al. (2009) Appion: An integrated, database-driven pipeline to facilitate EM image processing. *J Struct Biol* 166:95–102.
62. Rohou A, Grigorieff N (2015) CTFFIND4: Fast and accurate defocus estimation from electron micrographs. *J Struct Biol* 192:216–221.
63. Voss NR, Yoshioka CK, Radermacher M, Potter CS, Carragher B (2009) DoG Picker and TiltPicker: Software tools to facilitate particle selection in single particle electron microscopy. *J Struct Biol* 166:205–213.
64. Ludtke SJ, Baldwin PR, Chiu W (1999) EMAN: Semiautomated software for high-resolution single-particle reconstructions. *J Struct Biol* 128:82–97.
65. Scheres SH (2012) RELION: Implementation of a Bayesian approach to cryo-EM structure determination. *J Struct Biol* 180:519–530.
66. Hohn M, et al. (2007) SPARX, a new environment for Cryo-EM image processing. *J Struct Biol* 157:47–55.
67. Goddard TD, Huang CC, Ferrin TE (2007) Visualizing density maps with UCSF Chimera. *J Struct Biol* 157:281–287.